EPJ manuscript No.
(will be inserted by the editor)

Radiative π^0 photoproduction on protons in the $\Delta^+(1232)$ region

S. Schumann[1,2,a], B. Boillat[3], E.J. Downie[1,4], P. Aguar-Bartolomé[1], J. Ahrens[1], J.R.M. Annand[4], H.J. Arends[1], R. Beck[1,2], V. Bekrenev[5], A. Braghieri[6], D. Branford[7], W.J. Briscoe[8], J.W. Brudvik[9], S. Cherepnya[10], R. Codling[4], P. Drexler[11], L.V. Fil'kov[10] D.I. Glazier[7], R. Gregor[11], E. Heid[1], D. Hornidge[12], O. Jahn[1], V.L. Kashevarov[10], R. Kondratiev[13], M. Korolija[14], M. Kotulla[11], D. Krambrich[1], B. Krusche[3], M. Lang[1,2], V. Lisin[13], K. Livingston[4], S. Lugert[11], I.J.D. MacGregor[4], D.M. Manley[15], M. Martinez-Fabregate[1], J.C. McGeorge[4], D. Mekterovic[14], V. Metag[11], B.M.K. Nefkens[9], A. Nikolaev[1,2], R. Novotny[11], M. Ostrick[1], R.O. Owens[4], P. Pedroni[6], A. Polonski[13], S.N. Prakhov[9], J.W. Price[9], G. Rosner[4], M. Rost[1], T. Rostomyan[6], D. Sober[16], A. Starostin[9], I. Supek[14], C.M. Tarbert[7], A. Thomas[1], M. Unverzagt[1,2], Th. Walcher[1], D.P. Watts[7] and F. Zehr[3]

(Crystal Ball at MAMI, TAPS and A2 Collaborations)

[1] Institut für Kernphysik, Johannes Gutenberg-Universität Mainz, Mainz, Germany
[2] Helmholtz-Institut für Strahlen- und Kernphysik, Rheinische Friedrich-Wilhelms-Universität Bonn, Bonn, Germany
[3] Institut für Physik, Universität Basel, Basel, Switzerland
[4] Department of Physics and Astronomy, University of Glasgow, Glasgow, United Kingdom
[5] Petersburg Nuclear Physics Institute, Gatchina, Russia
[6] INFN Sezione di Pavia, Pavia, Italy
[7] School of Physics, University of Edinburgh, Edinburgh, United Kingdom
[8] Center for Nuclear Studies, The George Washington University, Washington, D.C., USA
[9] University of California at Los Angeles, Los Angeles, California, USA
[10] Lebedev Physical Institute, Moscow, Russia
[11] II. Physikalisches Institut, Justus Liebig-Universität Gießen, Gießen, Germany
[12] Mount Allison University, Sackville, NB, Canada
[13] Institute for Nuclear Research, Moscow, Russia
[14] Rudjer Boskovic Institute, Zagreb, Croatia
[15] Kent State University, Kent, Ohio, USA
[16] The Catholic University of America, Washington, D.C., USA

Received: date / Revised version: date

Abstract. The reaction $\gamma p \to p\pi^0\gamma'$ has been measured with the Crystal Ball / TAPS detectors using the energy-tagged photon beam at the electron accelerator facility MAMI-B. Energy and angular differential cross sections for the emitted photon γ' and angular differential cross sections for the π^0 have been determined with high statistics in the energy range of the $\Delta^+(1232)$ resonance. Cross sections and the ratio of the cross section to the non-radiative process $\gamma p \to p\pi^0$ are compared to theoretical reaction models, having the anomalous magnetic moment κ_{Δ^+} as free parameter. As the shape of the experimental distributions is not reproduced in detail by the model calculations, currently no extraction of κ_{Δ^+} is feasible.

PACS. 13.40.Em Electric and magnetic moments – 13.60.Le Meson production – 14.20.Gk Baryon resonances with $S = 0$ – 25.20.Lj Photoproduction reactions

1 Introduction

The $\Delta(1232)$ as a member of the $J^P = 3/2^+$ baryon decuplet acts as the first and only well-isolated resonance in elastic pion scattering or pion photproduction experiments. Its static electromagnetic properties, particularly the magnetic dipole moments μ_Δ, offer important tests for baryon structure calculations in the nonpertubative domain of QCD. Several predictions for the magnetic dipole moments of $\Delta(1232)$ isobars have been obtained (see table 1) using constituent quark based models [1,2,3] as well as lattice QCD calculations [4]. Recently, also the chiral extrapolation of latice results for μ_Δ including the next-to-leading nonanalytic (NLNA) structure of χPT was reported in ref. [5]. Since there are discrepancies between the different model calculations, experimental results for

[a] *E-mail address:* schumans@kph.uni-mainz.de

Table 1. Predictions of several baryon structure calculations for magnetic dipole moments of the $\Delta(1232)$ isobars.

Model	$\mu_{\Delta^{++}}/\mu_N$	$\mu_{\Delta^{+}}/\mu_N$	$\mu_{\Delta^{0}}/\mu_N$	$\mu_{\Delta^{-}}/\mu_N$
SU(6)	5.58	2.79	0.00	-2.79
RQM [1]	4.76	2.38	0.00	-2.38
χQSM [2]	5.40	2.65	-0.09	-2.83
χBM [3]	3.59	0.75	-2.09	-4.93
LQCD [4]	4.48 ± 0.30	2.24 ± 0.15	0.00	-2.24 ± 0.15
NLNA [5]	4.99 ± 0.56	2.49 ± 0.27	0.06	-2.45 ± 0.27

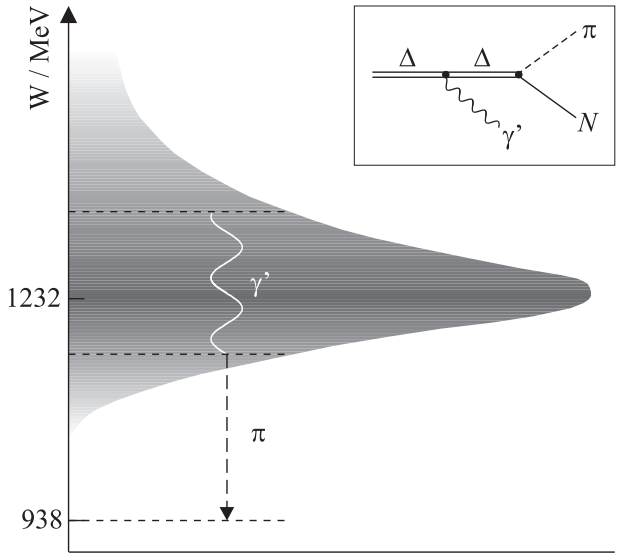

Fig. 1. Method of investigating electromagnetic moments of $\Delta(1232)$ baryons using a $\Delta \to \Delta\gamma'$ transition within the resonance width and a subsequent decay $\Delta \to N\pi$.

$\Delta(1232)$ magnetic dipole moments are desirable in order to constrain this observable at physical quark masses.

While experimental studies of the $N \to \Delta$ transition have provided access to electromagnetic transition moments (*e.g.* magnetic dipole $\mu_{N\to\Delta}$ and electric quadrupole $Q_{N\to\Delta}$ transition moments) [6,7], the static electromagnetic properties of the $\Delta(1232)$ itself, like μ_Δ and Q_Δ, are difficult to measure due to its short lifetime of about $\tau_\Delta \simeq 10^{-23}$ s. Thus, the experimental method of spin precession measurements of μ that have been performed with high precision for octet baryons (N, Λ, Σ, Ξ) as well as for the Ω^- decuplet baryon is not possible for short-lived states like the $\Delta(1232)$.

It has been proposed [8] to determine the magnetic dipole moment of the $\Delta(1232)$ from the measurement of electromagnetic transitions within the resonance width of $\Gamma_\Delta \simeq 120$ MeV. In this process the nucleon is excited to a Δ state, which then emits a real photon γ' and subsequently decays into a nucleon and a π meson (see fig. 1), hence leading to a $N\pi\gamma'$ final state. Because of spin and parity conservation, only $M1$, $E2$ and $M3$ multipoles are allowed for this $\Delta \to \Delta\gamma'$ transition. The amplitude for this process is dominated by magnetic dipole ($M1$) radiation and, therefore, proportional to μ_Δ, as higher multipole orders give only very small contributions. The electric quadrupole ($E2$) amplitude vanishes in the limit of zero photon energy due to time reversal symmetry [9] and furthermore the $E2/M1$ ratio of about -2.5% from the $N \to \Delta$ transition amplitude indicates that there is only a very small quadrupole deformation of the $\Delta(1232)$ [6]. Magnetic octupole ($M3$) radiation is suppressed by two additional powers of photon momentum with respect to the leading $M1$ order.

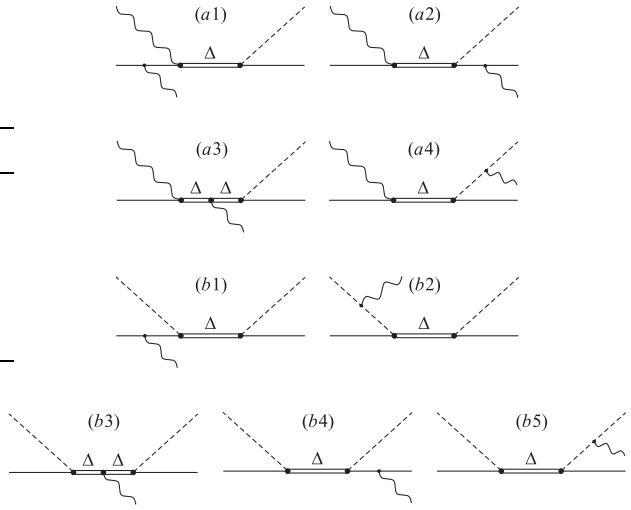

Fig. 2. Bremsstrahlung and Δ-resonant contributions to $N\pi\gamma'$ final states for pion photoproduction (a) and pion scattering (b). Only diagrams ($a3$) and ($b3$) are sensitive to the magnetic dipole moments μ_Δ.

Unfortunately, $N\pi\gamma'$ final states can also result from bremsstrahlung radiation emitted from incoming and outgoing protons or charged pions in $\pi N \to N\pi$ or $\gamma N \to N\pi$ processes (see fig. 2). Such contributions are of the same order as the $\Delta \to \Delta\gamma'$ transition and interfere with the process sensitive to μ_Δ. Thus, any interpretation of experimental results and determination of the magnetic dipole moment will require and rely on an accurate theoretical description of all reaction mechanisms contributing to $N\pi\gamma'$ final states.

This method for the determination of magnetic dipole moments of unstable particles was used for the first time in the 1970s at the Lawrence Berkeley National Laboratory (LBNL) [10,11] and some years later at the Schweizerisches Institut für Nuklearforschung / Paul Scherrer Institut (SIN / PSI) [12,13]. Both experiments used inelastic pion scattering $\pi^+ p \to p\pi^+\gamma'$ in order to extract the magnetic dipole moment $\mu_{\Delta^{++}}$ of the $\Delta^{++}(1232)$ isobar. As a result of several theoretical analyses [14,15,16,17] of both data sets, the Particle Data Group [18] quotes a range of $\mu_{\Delta^{++}} = 3.7$ to 7.5 μ_N, where $\mu_N = e\hbar/2m_N$ is the nuclear magneton. These large uncertainties are attributed to strong contributions mainly from π^+, but also from proton bremsstrahlung in this reaction channel and

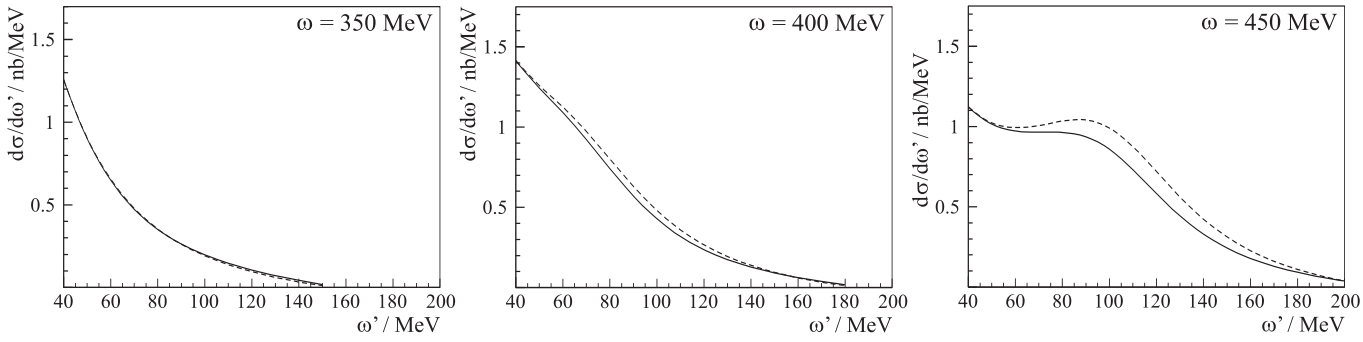

Fig. 3. Model calculations from ref. [9] for energy differential cross sections $d\sigma/d\omega'$ of the emitted photon γ' at different beam energies ω. Solid lines are predictions for an anomalous magnetic moment of $\kappa_{\Delta^+} = 3$, dashed lines are for $\kappa_{\Delta^+} = 0$.

model dependencies in the theoretical descriptions of the reaction.

In the case of the $\Delta^+(1232)$ a pioneering measurement of radiative π^0 photoproduction $\gamma p \to p\pi^0\gamma'$ was performed by the TAPS / A2 collaborations at MAMI [19] in 1999. From this experiment, together with the theoretical description of the reaction from ref. [9], a value of

$$\mu_{\Delta^+} = 2.7^{+1.0}_{-1.3}(\text{stat}) \pm 1.5(\text{syst}) \pm 3.0(\text{theo})\ \mu_N \qquad (1)$$

for the magnetic dipole moment of the $\Delta^+(1232)$ was extracted. The experimental precision of this result is limited by the poor statistics of around 500 reconstructed $\gamma p \to p\pi^0\gamma'$ events in the previous measurement and its quite large systematic uncertainties, resulting from an incomplete and inhomogeneous angular acceptance. Also, the theoretical reaction model from ref. [9] that was used to extract the result (1) for μ_{Δ^+} introduces further uncertainties due to model dependencies in the description of $\gamma p \to p\pi^0\gamma'$. Thus, a large improvement on the quality both of experimental data and theoretical descriptions is needed to get a value for μ_{Δ^+} that allows discrimination between different baryon structure calculations. In order to give a quantitative impression of the experimental and theoretical accuracies needed for the determination of μ_{Δ^+}, fig. 3 shows predictions for energy differential cross sections $d\sigma/d\omega'$ for the emitted photon γ' in the reaction $\gamma p \to p\pi^0\gamma'$. These are evaluated within the effective Lagrangian framework of ref. [9] using different values for the anomalous magnetic moment κ_{Δ^+}. From these curves it can be estimated that even in the favourable case at $\omega = 450$ MeV and assuming a precise model description of contributing reaction mechanisms, a relative experimental precision of about 10% is needed to get a determination of the magnetic dipole moment μ_{Δ^+} with an accuracy of approximately 0.5 to 0.8 μ_N, depending on details regarding the sensitivity to μ_{Δ^+} within a particular model framework.

This article presents new data on radiative π^0 photoproduction in the $\Delta^+(1232)$ energy region, measured with the Crystal Ball / TAPS detector set-up and the energy-tagged photon beam at the MAMI-B accelerator facility in Mainz. This detector system is described in sect. 2 and offers a much larger acceptance and efficiency than the TAPS photon spectrometer used in the previous $\gamma p \to p\pi^0\gamma'$ experiment. The data analysis and identification of $\gamma p \to p\pi^0\gamma'$ reactions are presented in sect. 3 together with a discussion of background contributions from π^0 and $\pi^0\pi^0$ production and sect. 4 gives an overview of different theoretical reaction models for radiative π^0 photoproduction. In sect. 5 the new experimental results for various cross sections and other observables are discussed and compared to predictions of these model calculations. Finally, our conclusions and a discussion of possible future developments are given in sect. 6.

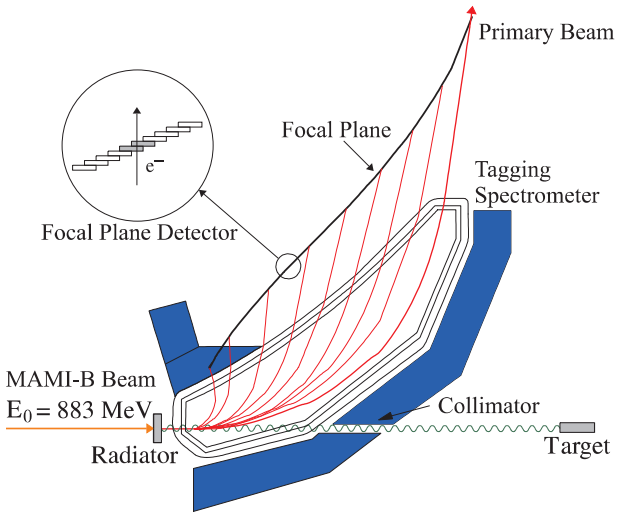

Fig. 4. Glasgow photon tagging system at MAMI-B, producing a quasi-monochromatic energy-tagged photon beam.

2 Experimental set-up

The reaction $\gamma p \to p\pi^0\gamma'$ has been measured at the Mainz Microtron (MAMI) electron accelerator facility [20] using the Glasgow tagging spectrometer [21,22] and the Crystal Ball / TAPS detector set-up. Bremsstrahlung photons are produced by scattering the 883 MeV MAMI-B electron beam on a 100 μm thick diamond radiator, while

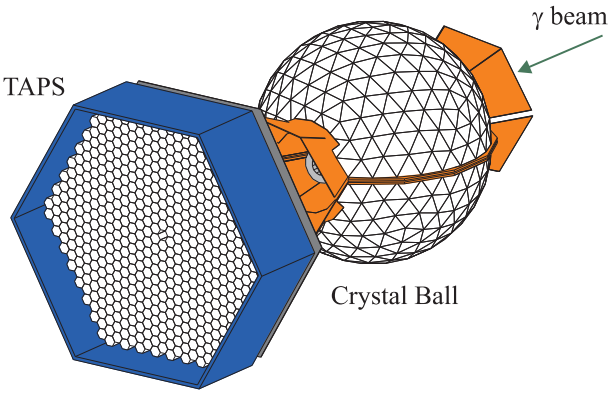

Fig. 5. Crystal Ball / TAPS detector set-up. Additional inner detector systems (PID, MWPCs) are installed inside the Crystal Ball beam tunnel.

scattered electrons are separated from the main beam and momentum-analysed by a magnetic dipole spectrometer and a focal plane detector system made of 353 half-overlapping plastic scintillators (see fig. 4). With the known beam energy E_0 and the energy E_e of scattered electrons the emitted photon energy ω is given by

$$\omega = E_0 - E_e \tag{2}$$

The resulting energy-tagged quasi-monochromatic photon beam covers an energy range from 208 to 820 MeV at an average energy resolution of $\Delta\omega \simeq 2$ MeV and a tagged photon flux of $2.8 \cdot 10^7$ s^{-1}. The photon flux is determined with an accuracy of about 5% by counting the scattered post-bremsstrahlung electrons with the focal plane detectors of the tagging system and correcting for the loss of emitted photons due to collimation. The probability for bremsstrahlung photons to reach the target ("tagging efficiency") is periodically measured by a total-absorption lead glass counter, which is moved into the photon beam line at reduced beam intensity. At 883 MeV electron beam energy and with a 3 mm diameter collimator, the tagging efficiency is approximately 34%.

The photon beam impinges on the target cell (length 4.76 cm) filled with liquid hydrogen and located in the centre of the Crystal Ball (CB) detector [23,24]. The Crystal Ball consists of 672 optically isolated NaI(Tl) crystals, each read out by an individual photomultiplier tube. Every crystal has the shape of a truncated triangular pyramid and is about 40.6 cm long, corresponding to 15.7 radiation lengths. The Crystal Ball covers the full azimuthal range and a polar angle range from 20° to 160°, resulting in a solid angle coverage of 93% of 4π. Electromagnetic showers are reconstructed with an energy resolution of $\sigma_E/E = 0.02/(E/\mathrm{GeV})^{1/4}$ and angular resolutions of $\sigma_\theta = 2°$ to 3° and $\sigma_\phi = \sigma_\theta/\sin\theta$ [24].

The target is surrounded by the cylindrical Particle Identification Detector (PID) made of 24 plastic scintillation counters aligned parallel to the beam axis. Each detector strip is 30 cm long and 2 mm thick. The PID measures the differential energy loss of charged particles, which together with the total energy deposited in the Crystal Ball, is used in a $\Delta E/E$ analysis for separation of protons and charged pions. To provide precise track reconstruction for charged particles, two cylindrical wire chambers (MWPCs) are placed between the PID and the Crystal Ball beam tunnel, covering a polar angle range from 21° to 159°. Directions of charged particles are reconstructed from the intersection points of the particle trajectories with the detection layers in both chambers, where angular resolutions of $\sigma_\theta = 1.3°$ to 2.3° and $\sigma_\phi = 1.4°$ and efficiencies of about 95% for protons and 85% for $\pi^\pm$ mesons are achieved. Angular resolutions for reconstructed tracks were determined from the passage of cosmic radiation through both chambers while efficiencies were obtained from analyses of $\gamma p \to p\pi^0$ and $\gamma p \to n\pi^+$ reactions.

Polar angles between 4° and 20° are covered by the TAPS detector [25,26] in a configuration with 510 BaF_2 modules arranged as a hexagonal forward wall at a distance of 1.75 m from the target centre. This results in a solid angle coverage of the combined Crystal Ball / TAPS detector set-up (see fig. 5) of around 97% of 4π. Each hexagonally shaped BaF_2 crystal has an inner diameter of 5.9 cm and a length of 25 cm, corresponding to 12 radiation lengths. Electromagnetic showers are determined with an energy resolution of $\sigma_E/E = 0.0079/(E/\mathrm{GeV})^{1/2} + 0.018$ and angular resolutions of less than 1° FWHM [26]. The two components of BaF_2 scintillation light (fast component with $\tau_\mathrm{f} = 0.7$ ns, slow component with $\tau_\mathrm{s} = 620$ ns) are separately digitised with different ADC gates and can be used in a pulse shape analysis (PSA) for particle identification. In front of each BaF_2 detector crystal a 5 mm thick plastic scintillator tile acts as a veto detector for charged particles.

With this set-up approximately 800 hours of data were taken in three run periods during 2004 and 2005. In addition about 120 hours of beam time were used for background measurements with empty target. Trigger conditions during all these runs were that the total deposited energy in the Crystal Ball is more than approximately 60 MeV and a combined sector multiplicity in the Crystal Ball and TAPS is three or more. For the Crystal Ball such a sector corresponds to a fixed group of 16 adjacent NaI(Tl) crystals, while TAPS is divided into four sectors, each consisting of either 127 or 128 BaF_2 modules. A sector contributes to the combined multiplicity if the deposited energy in at least one of its crystals exceeds a threshold of 15 MeV (Crystal Ball) or 25 MeV (TAPS). Additionally, an independent trigger condition (downscaled by a factor of 48) requiring a multiplicity of two or higher was used to record $\gamma p \to p\pi^0$ events for consistency checks and calibration purposes.

3 Data analysis

3.1 Radiative π^0 photoproduction

In the beam energy range up to 450 MeV radiative π^0 production has only a cross section of approximately 70 nb which is very small compared to $\gamma p \to p\pi^0$ and $\gamma p \to$

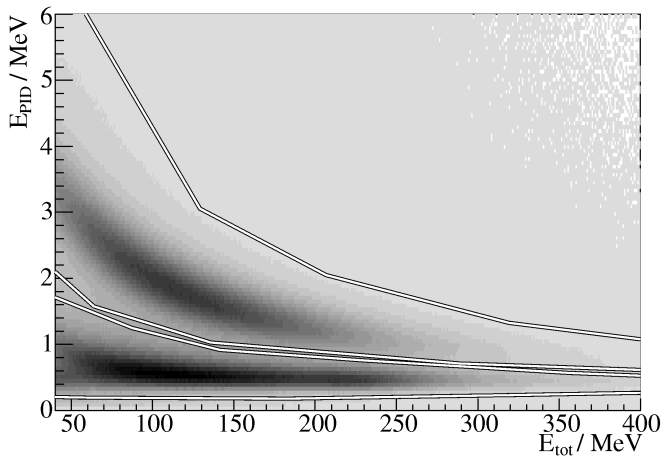

Fig. 6. $\Delta E/E$ analysis for charged particles detected in the Crystal Ball, using energy depositions $E_{\rm PID}$ and $E_{\rm tot}$ in PID strips and correlated NaI(Tl) clusters. Particles in the upper band are accepted as protons, particles in the lower band are accepted as $\pi^{\pm}$ mesons.

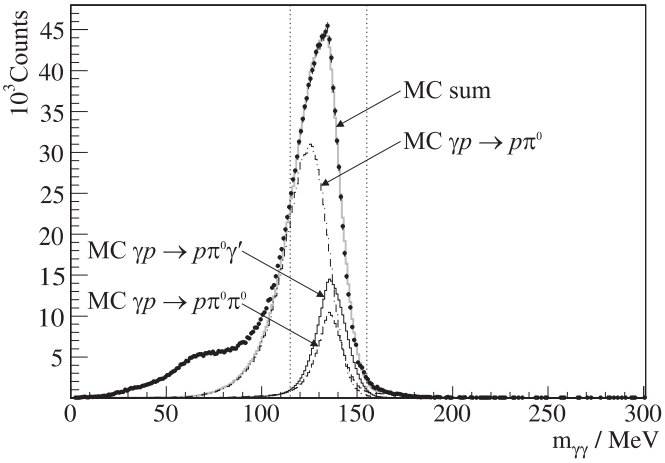

Fig. 7. Invariant $\gamma\gamma$ mass spectrum for the combination giving the smallest deviation from the π^0 mass. Data points represent experimental results, while the black lines are from MC simulations of $\gamma p \to p\pi^0$ (dashed-dotted), $\gamma p \to p\pi^0\gamma'$ (solid) and $\gamma p \to p\pi^0\pi^0$(dashed), respectively. For comparison with experimental data the sum of MC distributions is shown (grey solid line). Vertical lines indicate the accepted range for reconstructed π^0 masses.

$p\pi^0\pi^0$ reaction channels with cross sections of between 60 to 300 μb for single π^0 and up to 1 μb for double π^0 production. Under some circumstances these reactions can fake a $p\pi^0\gamma'$ final state in the detectors due to either loss of a decay photon in the double π^0 case or false detector hits in the single π^0 case. In order to separate the $\gamma p \to p\pi^0\gamma'$ reaction channel from such background contributions, an exclusive measurement of the $p\pi^0\gamma'$ final state has been performed. With measured 4-momenta of all particles, the reaction kinematics are overdetermined, allowing a variety of kinematic checks.

The first step in the $\gamma p \to p\pi^0\gamma'$ analysis is the selection of events with three neutral clusters and one cluster identified as a proton. For the Crystal Ball, charged particles are identified using azimuthal correlations between PID hits and clusters in the NaI(Tl) array. Further separation of protons and charged pions is done by comparing the energy loss $E_{\rm PID}$ in the PID strip and the total deposited energy $E_{\rm tot}$ from the correlated NaI(Tl) cluster ($\Delta E/E$ technique, see fig. 6). Precise direction information for protons detected in the Crystal Ball is obtained from tracks reconstructed using the MWPC data. Protons detected in the TAPS BaF_2 array are identified using the veto detector hits for separating charged and neutral particles and the pulse-shape information available from short- and long-gate ADC data.

Measured proton energies are corrected for energy loss in the target and inner detector systems as well as for different shower propagation compared to photons in the detector materials. This is done by applying a correction function obtained from exclusive measurements of $\gamma p \to p\pi^0$ reactions, where measured proton energies can be compared to expected energies calculated from two-body kinematics.

The π^0 meson is identified and reconstructed from its decay into two photons, using the invariant mass $m_{\gamma\gamma}$ as the selection criterion. As the reaction $\gamma p \to p\pi^0\gamma'$ leads to a three-photon final state, three different permutations from two out of these three photons are possible ($\gamma_1\gamma_2$, $\gamma_1\gamma_3$, $\gamma_2\gamma_3$). Therefore, photons from the combination resulting in an invariant mass with the smallest deviation from the π^0 mass are assigned to be π^0 decay photons, with the remaining one being interpreted as γ'. The distribution of invariant masses for the best photon combination is shown in fig. 7 together with spectra obtained from MC simulations of the $\gamma p \to p\pi^0$, $\gamma p \to p\pi^0\gamma'$ and $\gamma p \to p\pi^0\pi^0$ reaction channels. The experimental distribution is dominated by background from non-radiative single π^0 production, where a secondary particle from an electromagnetic shower separates and travels some distance in the detector before interacting with material and creating an additional hit ("split-off") outside the primary cluster. In these cases, part of the original photon 4-momentum is not taken into account, which explains the shift to smaller invariant $\gamma\gamma$ masses in the case of $\gamma p \to p\pi^0$ background contributions. The low-energy background contribution at masses $m_{\gamma\gamma} < 100$ MeV originates from electromagnetic background processes from the photon beam and, therefore, is not reproduced by simulations of π^0 photoproduction channels. Such contributions are, however, removed by the condition 115 MeV $< m_{\gamma\gamma} <$ 155 MeV for reconstructed π^0 masses.

Because of the large background contribution from non-radiative single π^0 production, candidates for $\gamma p \to p\pi^0\gamma'$ events are explicitly tested for the two-body kinematics of $\gamma p \to p\pi^0$ reactions. For the π^0 meson the missing energy

$$E_{\rm miss}(\pi^0) = E^*_\pi - \frac{s + m_\pi^2 - m_p^2}{2W} \qquad (3)$$

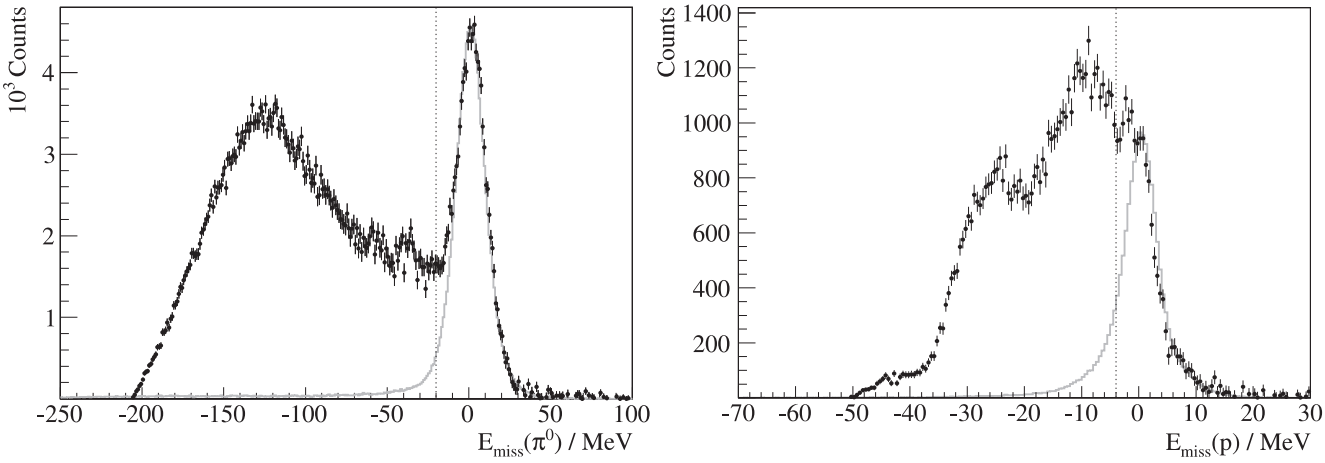

Fig. 8. Missing energy spectra for reconstructed π^0 mesons (left) and protons (right) under the assumption of a $\gamma p \to p\pi^0$ reaction. Data points represent results for $\gamma p \to p\pi^0\gamma'$ candidates; for comparison, the grey solid lines show experimental distributions obtained from identified $\gamma p \to p\pi^0$ events. Events resulting in missing energies right of the vertical lines are interpreted as $\gamma p \to p\pi^0$ reactions.

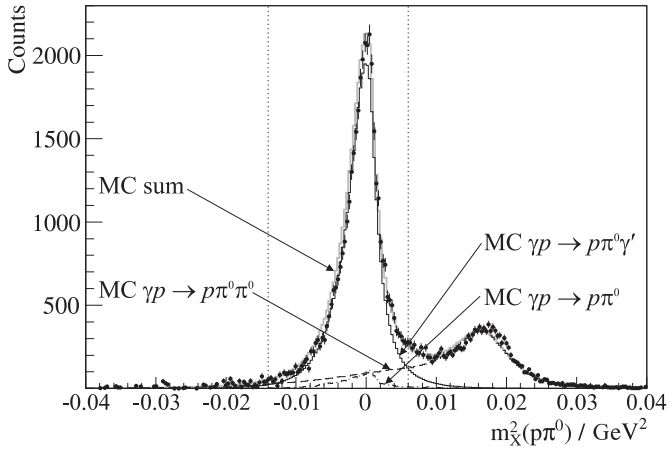

Fig. 9. Missing mass spectrum calculated from the $p\pi^0$ system. The peak around $m_{\mathrm{X}}^2 = 0.0182$ GeV^2 corresponds to the mass of a second π^0. Data points represent experimental results, while the black lines are from MC simulations of $\gamma p \to p\pi^0$ (dashed-dotted), $\gamma p \to p\pi^0\gamma'$ (solid) and $\gamma p \to p\pi^0\pi^0$(dashed), respectively. For comparison with experimental data the sum of MC distributions is also shown (grey solid line). Vertical lines indicate the accepted range for missing γ' masses.

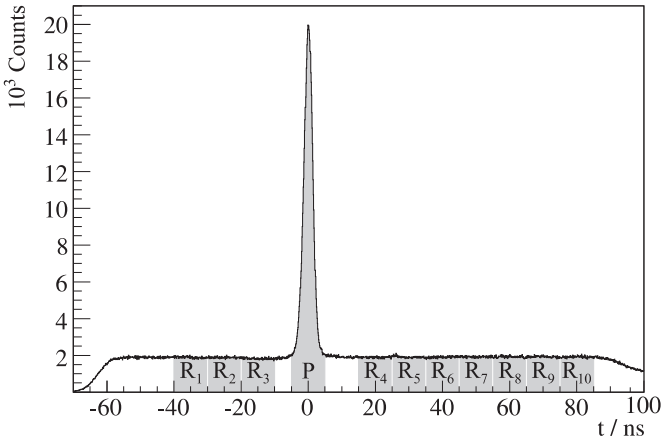

Fig. 10. Time coincidence between Crystal Ball / TAPS and tagging system. Random coincidences are evaluated from background windows R_i and subtracted from events located within the prompt coincidence window P.

is calculated, where E_π^* denotes the measured π^0 energy in the c.m. frame, m_π and m_p are the π^0 and proton masses, respectively, and

$$W = \sqrt{s} = \sqrt{m_p^2 + 2\omega m_p} \qquad (4)$$

is the total c.m. energy at a given photon beam energy ω. Values around $E_{\mathrm{miss}}(\pi^0) = 0$ MeV indicate events from $\gamma p \to p\pi^0$ reactions, where the measured π^0 energy corresponds to the expected value calculated from two-body kinematics (see fig. 8). An analogous calculation is done subsequently for the missing energy $E_{\mathrm{miss}}(p)$ of the proton, and all events not fulfilling both the conditions $E_{\mathrm{miss}}(\pi^0) < -20$ MeV and $E_{\mathrm{miss}}(p) < -4$ MeV are interpreted as $\gamma p \to p\pi^0$ background.

Double π^0 production events can lead to three-photon final states if a decay photon escapes detection either due to the incomplete angular acceptance or, in case of a highly asymmetric π^0 decay, the photon energy falls below the detection threshold of about 25 MeV. Such events are identified using a missing mass analysis of the detected $p\pi^0$ system without taking into account the additional photon γ'. The mass m_{X} of the third final-state particle is calculated from

$$m_{\mathrm{X}}^2(p\pi^0) = (\omega + m_p - E_\pi - E_p)^2 - (\boldsymbol{k} - \boldsymbol{q}_\pi - \boldsymbol{p}_p)^2 \qquad (5)$$

where ω, $\boldsymbol{k}$ denote energy and momentum of the beam photon, while the energies and momenta of proton and

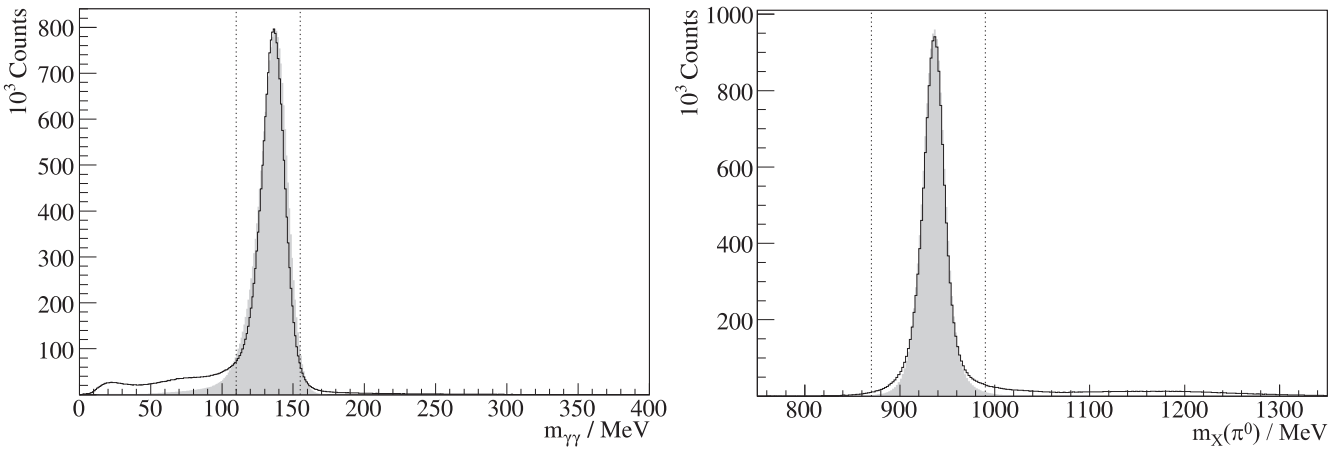

Fig. 11. Analysis of $\gamma p \to p\pi^0$ reactions. Left: Invariant $\gamma\gamma$ mass spectrum for events with two photons. Right: Missing mass spectrum calculated from the reconstructed π^0. Solid lines represent experimental results, while the grey shaded distributions are from a MC simulation of $\gamma p \to p\pi^0$ normalised to the experimental peak maximum. Vertical lines indicate the ranges of π^0 and proton mass values accepted for further analysis.

Table 2. Background contributions from simulated single and double π^0 production reactions to the number of reconstructed events fulfilling the analysis conditions for $\gamma p \to p\pi^0\gamma'$.

Beam energy ω	Total events	Single π^0 background	Double π^0 background
350 MeV	5880	355	3
400 MeV	11996	345	66
450 MeV	11839	224	1139

π^0 in the final state are given by E_p, $\boldsymbol{p}_p$ and E_π, $\boldsymbol{q}_\pi$. For double π^0 production the mass of the second π^0 is reproduced, leading to a peak around $m_X^2 = 0.0182$ GeV^2 (see fig. 9), while for $\gamma p \to p\pi^0\gamma'$ the expected value for the squared missing mass is around $m_X^2 = 0$ GeV^2, corresponding to the mass of the photon γ'. Thus, events with a squared missing mass in the range -0.014 GeV$^2 < m_X^2 < 0.006$ GeV^2 are accepted as $\gamma p \to p\pi^0\gamma'$ reactions.

Finally, remaining random time coincidences between the tagging system and the Crystal Ball / TAPS detector setup are subtracted. These are determined from background events outside the prompt coincidence peak (see fig. 10). Choosing the same width for prompt and random windows makes sure that timing conditions are the same for all events. Random coincidences are evaluated from different time regions R_1 to R_{10} to get a larger sample of background events and reduce the statistical errors.

Several GEANT 3.21 based MC simulations were performed to determine detector acceptance and efficiency as well as the remaining background contributions. Kinematic distributions for $\gamma p \to p\pi^0\gamma'$ were generated using predictions from ref. [9] for five-fold differential cross sections $\mathrm{d}^5\sigma/\mathrm{d}\omega'\mathrm{d}\Omega_{\gamma'}\mathrm{d}\Omega_\pi$ at different beam energies. Simulations using different values of κ_{Δ_+} were performed to ensure that efficiencies do not depend on the anomalous magnetic moment used as input for the reaction model. With these simulations the overall detection and reconstruction efficiency has been determined to be about 13.5% for an exclusive measurement of the $p\pi^0\gamma'$ final state. The simulation of $\gamma p \to p\pi^0$ background reactions is based on MAID [27,28] calculations for differential cross sections $\mathrm{d}\sigma/\mathrm{d}\Omega_\pi$ at different beam energies, while for $\gamma p \to p\pi^0\pi^0$ a phase-space distribution together with a beam energy dependence according to the total cross section $\sigma_{\pi\pi}$ from ref. [29] is used. These simulations show that the remaining background contributions are approximately 3% from non-radiative single π^0 and 4% from double π^0 production. Background from $\gamma p \to p\pi^0\pi^0$ appears mainly at higher beam energies around 450 MeV, where it rises up to about 10%, while at lower beam energies only a negligible contribution is observed (see table 2). The absolute background contribution is derived from kinematic distributions like fig. 9 and is checked for consistency with the acceptances for $\gamma p \to p\pi^0$ and $\gamma p \to p\pi^0\pi^0$ in combination with the particular total cross sections for both reactions.

For the determination of cross sections the simulated background is subtracted from the experimental results, leading to a total number of about 27600 reconstructed radiative π^0 photoproduction events. Cross sections are calculated from this number of reconstructed $\gamma p \to p\pi^0\gamma'$ events, corrected for detection and analysis efficiency and normalised to the number of target protons per cm^2 and the incoming photon beam flux. In order to account for contributions from the target cell material (125 μm Kapton) that have been found to be of the order of 2%, cross sections are evaluated in the same way for data taken with an empty target and subsequently subtracted from the full target results.

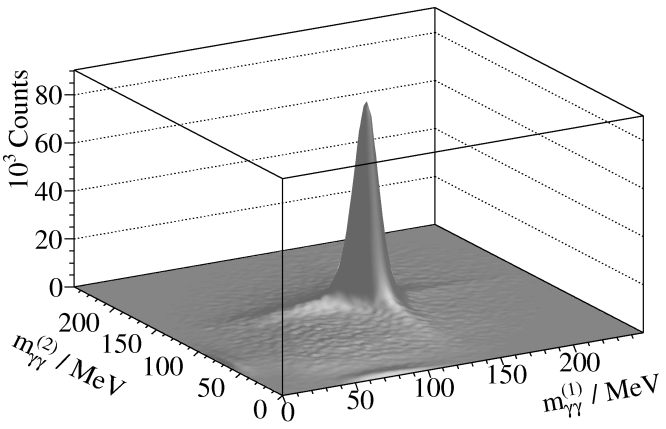

Fig. 12. Invariant masses of $\gamma\gamma$ pairs for double π^0 production. Only the best combination with minimal χ^2 according to eq. (7) is shown.

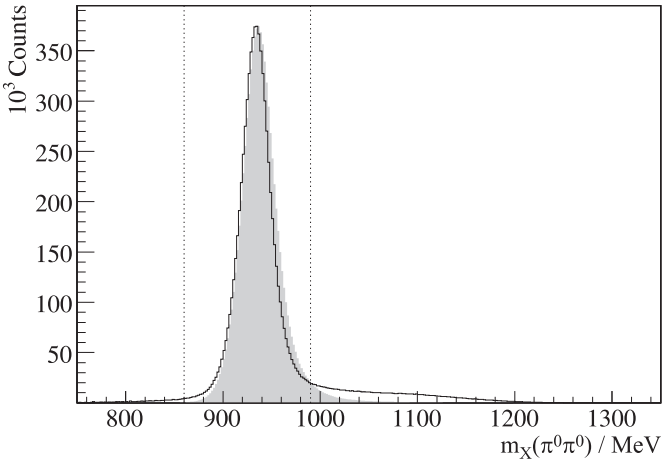

Fig. 13. Missing mass spectrum for double π^0 production. The solid line represents experimental results, while the grey shaded distribution is from a MC simulation of $\gamma p \to p\pi^0\pi^0$ normalised to the experimental peak maximum. Vertical lines indicate the accepted ranges for missing proton masses.

3.2 Single and double π^0 photoproduction

In addition to the $\gamma p \to p\pi^0\gamma'$ analysis cross sections for non-radiative single and double π^0 production reactions have also been extracted from the experimental data. As these processes form the major background contributions for $\gamma p \to p\pi^0\gamma'$, a quantitative understanding of $\gamma p \to p\pi^0$ and $\gamma p \to p\pi^0\pi^0$ is desirable and can be used to check the consistency of calibrations and data analysis.

The analysis of single π^0 production has been limited to events fulfilling the downscaled trigger condition that the sector multiplicity is two or more. From this dataset events with two neutral clusters are selected and the π^0 is identified and reconstructed using the invariant mass $m_{\gamma\gamma}$ of the photon pair (see left panel of fig. 11). The identification of the $\gamma p \to p\pi^0$ reaction channel is then done by evaluating the missing mass

$$m_{\mathrm{X}}(\pi^0) = \sqrt{(\omega + m_p - E_\pi)^2 - (\boldsymbol{k} - \boldsymbol{q}_\pi)^2} \qquad (6)$$

(see right panel of fig. 11), where ω, $\boldsymbol{k}$ and E_π, $\boldsymbol{q}_\pi$ denote energy and momentum of the beam photon and the reconstructed π^0, respectively. To determine the total cross section, random and empty target background is subtracted and the MAID-based MC simulation of $\gamma p \to p\pi^0$, as described above, is used to correct the number of reconstructed events for detection and analysis efficiency, which is about 67% for an inclusive measurement of single π^0 production. The total systematic uncertainty for this reaction is estimated to be about 6%, which covers uncertainties of 5% in photon flux determination and 1.8% for target length and density as well as 3% for acceptance and efficiency corrections.

In the case of double π^0 production events with four detected photons are selected and the π^0 mesons are reconstructed from the best combination of $\gamma\gamma$ pairs. As there are 3 different possible permutations, the combination with the best simultaneous reconstruction of both pions, *i.e.* with minimal

$$\chi^2 = \left(m^{(1)}_{\gamma\gamma} - m_\pi\right)^2 + \left(m^{(2)}_{\gamma\gamma} - m_\pi\right)^2 \qquad (7)$$

is selected (see fig. 12). Similar to the single π^0 case, the final identification of the reaction channel $\gamma p \to p\pi^0\pi^0$ is done using the missing mass (see fig. 13) calculated from the reconstructed π^0 mesons according to

$$m_{\mathrm{X}}(\pi^0\pi^0) = \sqrt{\left(k + p_{\mathrm{T}} - q^{(1)}_\pi - q^{(2)}_\pi\right)^2} \qquad (8)$$

where $k = (\omega, \boldsymbol{k})$ and $p_{\mathrm{T}} = (m_p, \boldsymbol{0})$ denote the 4-momenta of the initial beam photon and target proton, while the 4-momenta of the final state pions are given by $q_\pi = (E_\pi, \boldsymbol{q}_\pi)$. After subtraction of empty target and random background contributions, the total cross section is calculated using the detection and reconstruction efficiency of about 42% for the inclusive case, determined with the phase-space MC simulation described above. Kinematic discrepancies between simulation and experimental data are taken into account in the systematic uncertainty of the efficiency correction, which is estimated to be 5%. Together with the absolute normalisation uncertainties from photon flux and target density, which are the same as for the single π^0 case, this gives a total systematic uncertainty of about 7% for the double π^0 production cross sections.

4 Reaction models

In order to determine the $\Delta^+(1232)$ magnetic dipole moment μ_{Δ^+} from experimental results for $\gamma p \to p\pi^0\gamma'$ an accurate theoretical description of all contributing processes is required. While first theoretical calculations [30,31,32] considered only the Δ-resonant mechanism and, therefore,

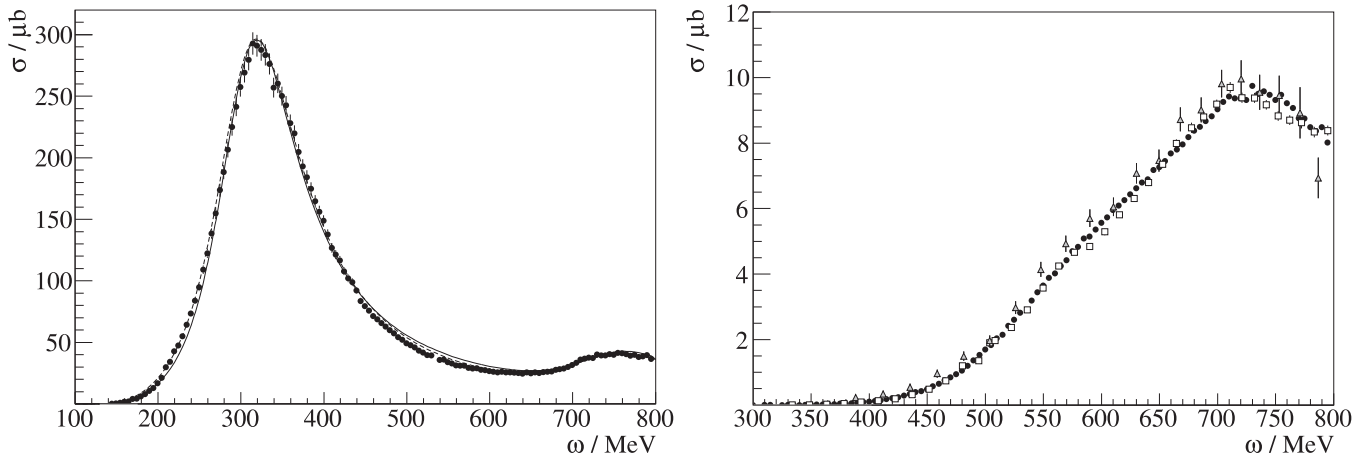

Fig. 14. Total cross sections for background reactions $\gamma p \to p\pi^0$ (left) and $\gamma p \to p\pi^0\pi^0$ (right). Black points represent Crystal Ball / TAPS results, black lines show MAID [27,28] (solid) and SAID [38] (dashed) predictions for single π^0 production. White squares and grey triangles are double π^0 results from refs. [39] and [40], respectively. Error bars include both statistical and systematic uncertainties for $\gamma p \to p\pi^0$ and statistical uncertainties only for $\gamma p \to p\pi^0\pi^0$.

could not reproduce experimental results, an extended description including several other contributions has been presented in ref. [9]. This model was used for the extraction of μ_{Δ^+} from the previous TAPS / A2 experiment in ref. [19]. Its calculations are done within the context of an effective Lagrangian formalism, where in the first step the Δ-resonant mechanism as well as a background of non-resonant contributions (Born terms, vector meson exchange) are taken into account for a tree-level description of the $\gamma p \to p\pi^0$ process. Then, the additional photon γ' is coupled in a gauge-invariant way to charged particles, leading to the $\gamma p \to p\pi^0\gamma'$ reaction and introducing the anomalous magnetic moment κ_{Δ^+} as a new parameter to the $\gamma\Delta\Delta$ vertex, where μ_{Δ^+} and κ_{Δ^+} are related according to

$$\mu_{\Delta^+} = (1 + \kappa_{\Delta^+}) \frac{e\hbar}{2m_\Delta} = (1 + \kappa_{\Delta^+}) \frac{m_N}{m_\Delta} \mu_N \qquad (9)$$

with m_N and m_Δ the nucleon and $\Delta^+(1232)$ masses, respectively.

Since the earlier determination of μ_{Δ^+} several improvements have been made to the theoretical calculations. The effective Lagrangian approach from ref. [9] has been extended in ref. [33] to a unitarised dynamical model of $\gamma p \to N\pi\gamma'$ reactions (in the following referred to as "unitary model"), including πN rescattering effects in an on-shell approximation for intermediate particles (K matrix approximation). Furthermore these rescattering contributions are treated in the soft-photon limit $\omega' \to 0$ for the final γ', where the T matrix for $\gamma p \to N\pi\gamma'$ reactions is directly proportional to the full T matrix for $\gamma p \to N\pi$ processes.

In another approach, descriptions of radiative pion photoproduction $\gamma p \to N\pi\gamma'$ using chiral effective field theory (χEFT) have been developed [34,35] in order to use a more consistent and systematic framework compared to the "phenomenological" effective Lagrangian models from

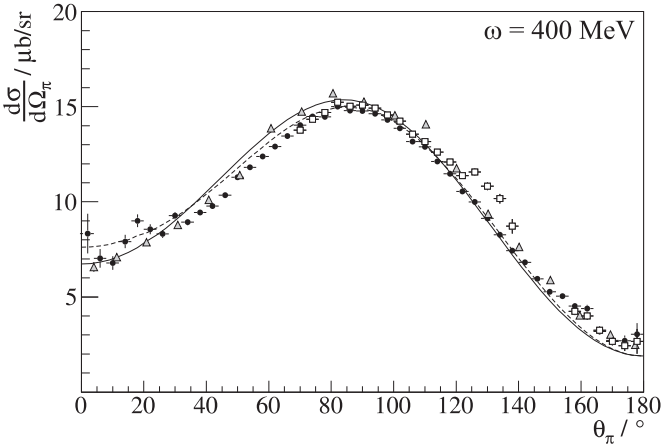

Fig. 15. Differential cross section $d\sigma/d\Omega_\pi$ for $\gamma p \to p\pi^0$. Black points and white squares represent Crystal Ball / TAPS results for inclusive (π^0 only) and exclusive (p and π^0) measurements, respectively, while grey triangles are results from ref. [41]. Black lines show MAID [27,28] (solid) and SAID [38] (dashed) predictions. Error bars include statistical uncertainties only.

refs. [9] and [33]. The framework of χEFT allows the calculation of chiral loop corrections in a consistent way following quantum field theory, where the chiral symmetry of the low-energy strong interaction as well as other general principles like unitarity and analyticity are included to any given order in a systematic expansion over the energy scales and hadronic degrees of freedom. The latest calculations in ref. [35] are based on a next-to-leading order (NLO) chiral expansion with Δ-isobar degrees of freedom (using the δ-expansion power counting scheme described in refs. [36,37]) and a next-next-to-leading order (NNLO) soft-photon expansion with respect to the emitted γ' energy, since this is the order at which μ_{Δ^+} first appears.

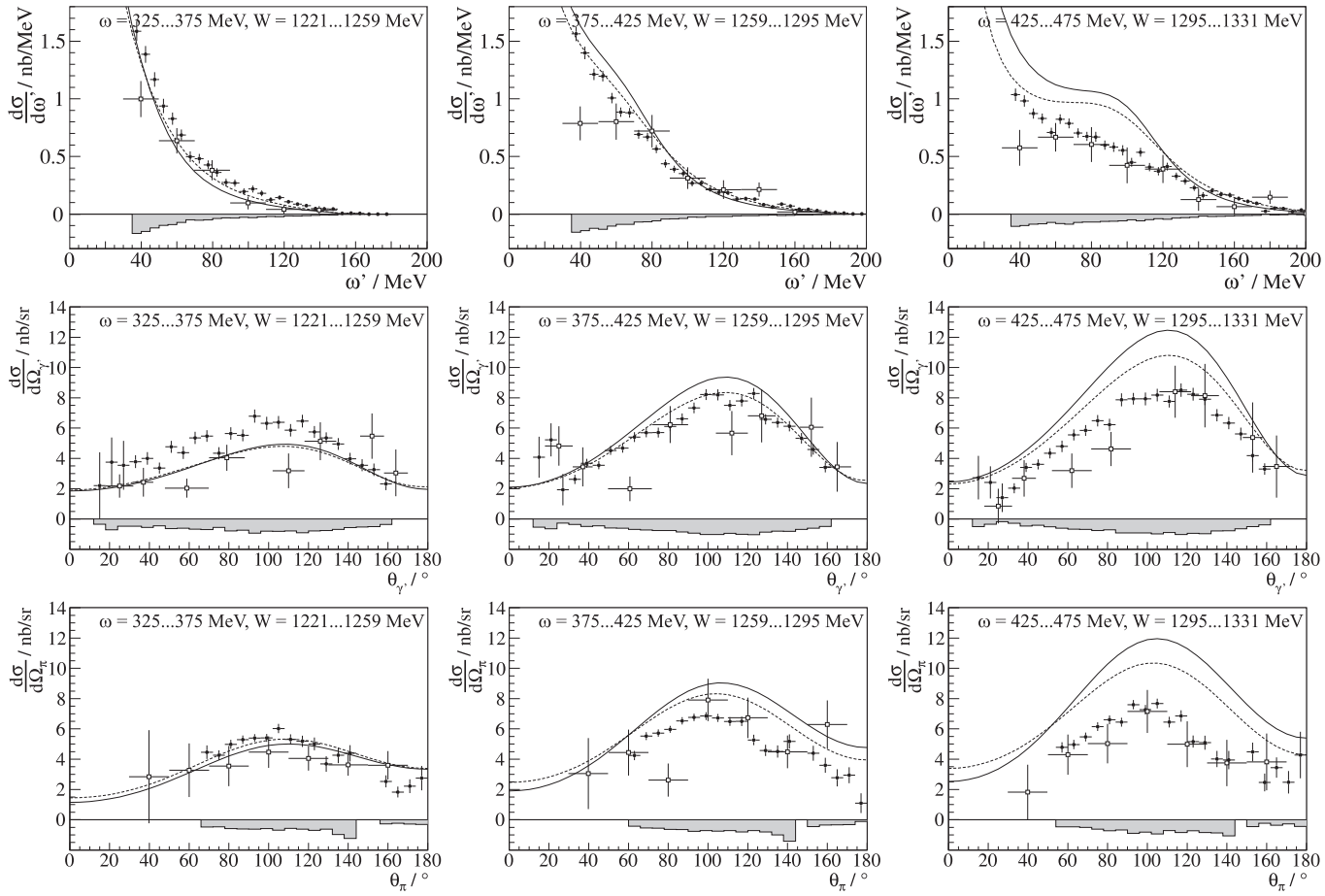

Fig. 16. Differential cross sections at different ranges for beam energy ω and total c.m. energy W, respectively. Black points represent Crystal Ball / TAPS results, white squares are results from ref. [19]. Error bars denote statistical errors, grey shaded bands show absolute systematic uncertainties. Black lines are theoretical predictions (using $\kappa_{\Delta^+} = 2.6$) of the unitary model from ref. [33] (dashed line) and the χEFT calculation from ref. [35] (solid line). Top: Energy differential cross section $\mathrm{d}\sigma/\mathrm{d}\omega'$ for the emitted photon γ'. Middle: Angular differential cross section $\mathrm{d}\sigma/\mathrm{d}\Omega_{\gamma'}$ for the emitted photon γ'. Bottom: Angular differential cross section $\mathrm{d}\sigma/\mathrm{d}\Omega_\pi$ for the reconstructed π^0 meson.

5 Results and discussion

5.1 Single and double π^0 photoproduction

Before discussing our new experimental results for radiative π^0 photoproduction we also present total cross sections for $\gamma p \to p\pi^0$ and $\gamma p \to p\pi^0\pi^0$ reactions obtained with the data analysis as described in sect. 3. Figure 14 shows the total cross sections for single and double π^0 production in the energy range from the particular thresholds up to a beam energy of 800 MeV. For $\gamma p \to p\pi^0$ the new Crystal Ball / TAPS results show good agreement with recent calculations from MAID [27,28] and SAID [38] multipole analyses that reproduce all recent data for differential and total π^0 photoproduction cross sections up to 800 MeV. Results for double π^0 production are compared to two previous measurements from refs. [39] and [40] with the TAPS and DAPHNE detectors, respectively. The overall agreement with both older data sets is rather good. The small differences are attributed to the phase-space-based efficiency corrections and covered by the systematic uncertainties. These are estimated to be 10% for the previous TAPS data, 4% for the DAPHNE measurement and 7% for our new results.

In addition, fig. 15 shows the differential cross section $\mathrm{d}\sigma/\mathrm{d}\Omega_\pi$ for both inclusive and exclusive measurements of $\gamma p \to p\pi^0$. In the inclusive analysis, as described above, only the π^0 has been reconstructed from its decay into two photons, while for the exclusive case the recoil proton has also been detected and identified. This limits the angular acceptance due to detection limitations for the proton (*e.g.* a minimum kinetic energy of $T_p \simeq 50$ MeV in the lab frame) to approximately $\theta_\pi = 70°$ to $140°$ and $\theta_\pi > 155°$, where protons are detected in the Crystal Ball and TAPS, respectively. The acceptance gap between both detectors is caused mainly by additional material of the inner detector readout electronics, which blocks the lab frame range from about $\theta = 10°$ to $20°$ for charged particles. As this gives an inhomogeneous and complicated acceptance, any remaining charged particles within this angular range are

discarded in the analysis. Both the inclusive and the exclusive results agree rather well with each other and also with a previous TAPS / A2 measurement of $\gamma p \to p\pi^0$ from ref. [41] except for π^0 polar angles around $\theta_\pi = 130°$. These deviations are attributed to inhomogeneities in the proton acceptance resulting from the complicated geometry of the Crystal Ball beam tunnel region. The total discrepancy between inclusive and exclusive measurements is about 4%, which is taken into account as an additional systematic uncertainty for the proton reconstruction efficiency. In general, the good agreement of our results with model predictions and previous experiments for single and double π^0 production indicates that a reasonable understanding of the main background contributions to $\gamma p \to p\pi^0\gamma'$ reactions has been achieved.

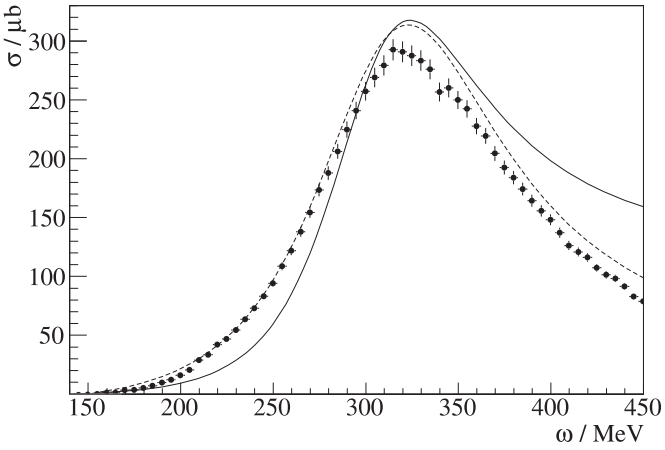

Fig. 17. Total cross section for $\gamma p \to p\pi^0$ in the energy region of the $\Delta^+(1232)$. Data points represent Crystal Ball / TAPS results, error bars include both statistical and systematic uncertainties. Dashed and solid lines show predictions from the unitarised effective Lagrangian model [33] and the χEFT calculation [35], respectively.

5.2 Radiative π^0 photoproduction

For radiative π^0 production in the $\gamma p \to p\pi^0\gamma'$ reaction, fig. 16 shows energy and angular differential cross sections for the emitted photon γ' as well as angular differential cross sections for the π^0 meson. These cross sections have been determined for three different beam energy bins, corresponding to c.m. energies $W = \sqrt{s}$ starting close to the $\Delta^+(1232)$ resonance position and increasing to 100 MeV above. All cross sections that are not differential in γ' energy are integrated over $\omega' > 30$ MeV. Systematic uncertainties that are shown as shaded error bands in fig. 16 include uncertainties in absolute normalisation, namely 5% for photon flux and 1.8% for target density, as well as uncertainties in efficiency correction. This covers discrepancies between simulated and experimental kinematic distributions, giving an energy- and angular-dependent contribution to the acceptance uncertainty which is, on average, around 7%. Furthermore, a 4% uncertainty for proton reconstruction in exclusive measurements is taken into account, as described above. Finally, for subtraction of single and double π^0 background a systematic uncertainty of 7.5% in the number of subtracted events is assumed. Quadratic addition of all contributions then results in a mean value of aproximately 10% for the systematic uncertainties on the measured cross sections for $\gamma p \to p\pi^0\gamma'$.

The energy differential cross sections $\mathrm{d}\sigma/\mathrm{d}\omega'$ in the upper panels of fig. 16 are dominated by a $1/\omega'$ behaviour as expected from bremsstrahlung contributions of the initial and final protons, although, especially in the highest beam energy interval, this shape is slightly modified by a broad distribution of emitted photon energies around $\omega' = 80$ MeV, caused by interference between proton bremsstrahlung and the Δ-resonant process. Both theoretical models seem to overestimate this effect and predict a pronounced peak in this energy range, which is not clearly visible in the experimental results. Compared to the existing data from ref. [19] the agreement is good, except for the low-energy region around emitted photon energies of $\omega' = 40$ MeV, where the previous measurement resulted in significantly smaller cross sections.

The angular differential cross sections $\mathrm{d}\sigma/\mathrm{d}\Omega_{\gamma'}$ show a broad distribution with a maximum around photon polar angles of about 110° (see middle panels of fig. 16). This is caused by interference between bremsstrahlung from the initial and final protons and the Δ-resonant mechanism, while a pure Δ-resonant process would produce an angular distribution peaking at 90°. Both model calculations in general reproduce the shape of the angular distributions but overestimate the absolute cross sections at higher beam energies, while there is reasonable agreement between the old TAPS / A2 measurement and our new data.

Angular distributions $\mathrm{d}\sigma/\mathrm{d}\Omega_\pi$ for the π^0 meson have been determined for polar angles in the range from $\theta_\pi = 60°$ to 140° and $\theta_\pi > 150°$ (see lower panels of fig. 16). As in the analysis of $\gamma p \to p\pi^0\gamma'$ reactions any charged particles within the laboratory polar angle range between 10° and 20° are discarded due to the complicated acceptance in this region. This is comparable to the single π^0 case (see fig. 15), as the kinematics for $\gamma p \to p\pi^0\gamma'$ are very similar to $\gamma p \to p\pi^0$ especially for soft photons γ' resulting from the dominating proton bremsstrahlung. Also for this observable, the cross section shape is reproduced quite well by theoretical calculations, but the the discrepancies in the absolute values increase more and more with rising beam energy.

These discrepancies in the cross section predictions are mainly attributed to inaccuracies in the description of the non-radiative $\gamma p \to p\pi^0$ reaction (see fig. 17), which is connected to the $\gamma p \to p\pi^0\gamma'$ process by the low-energy theorem for $\omega' \to 0$. This is particularly important for the χEFT calculation from ref. [35], that does not include any vector meson (ρ, ω) exchange mechanisms. These processes, however, dominate the high-energy behaviour of $\gamma p \to p\pi^0$, where the Δ excitation alone yields cross sections that are too large and are subsequently reduced by the addition of ρ, ω exchange mechanisms. Some of these model dependencies can be avoided by construction of a

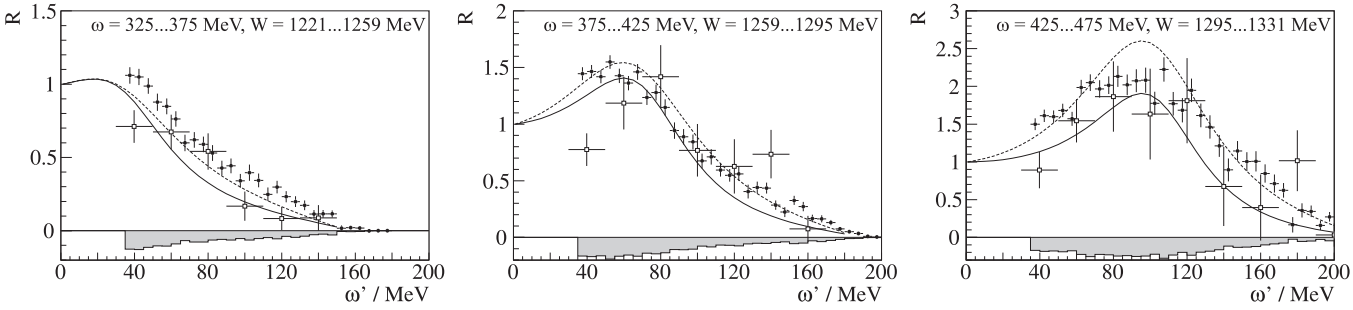

Fig. 18. Cross section ratio R at different ranges for beam energy ω and total c.m. energy W, respectively. Black points represent Crystal Ball / TAPS results, white squares are results from ref. [19]. Error bars denote statistical errors, grey shaded bands show absolute systematic uncertainties. Black lines are theoretical predictions (using $\kappa_{\Delta^+} = 2.6$) of the unitary model from ref. [33] (dashed line) and the χEFT calculation from ref. [35] (solid line).

suitable observable for $\gamma p \to p\pi^0\gamma'$ that does not depend on details of the $\gamma p \to p\pi^0$ reaction description.

In the soft-photon limit ($\omega' \to 0$) radiative π^0 production is completely determined by bremsstrahlung processes from the initial and final protons and gauge invariance provides a model-independent relation between $\gamma p \to p\pi^0\gamma'$ and non-radiative $\gamma p \to p\pi^0$ reactions. As shown in ref. [42], in this soft-photon limit the three-fold differential cross section, after integration over the outgoing photon angles, is given by

$$\frac{\mathrm{d}^3\sigma}{\mathrm{d}\omega'\mathrm{d}\Omega_\pi} \overset{\omega'\to 0}{\longrightarrow} \frac{1}{\omega'} \cdot \frac{e^2}{2\pi^2} \cdot W(v) \cdot \frac{\mathrm{d}\sigma}{\mathrm{d}\Omega_\pi} \tag{10}$$

with $\mathrm{d}\sigma/\mathrm{d}\Omega_\pi$ being the differential cross section for the $\gamma p \to p\pi^0$ process, and an angular weight function

$$W(v) = \left(\frac{v^2+1}{2v}\right) \cdot \ln\left(\frac{v+1}{v-1}\right) - 1 \tag{11}$$

with

$$v = \sqrt{1 - \frac{4m_p}{(k-q)^2}} \tag{12}$$

where k, q denote the 4-momenta of the beam photon and the π^0, respectively. Integration over the meson angles yields an energy distribution

$$\frac{\mathrm{d}\sigma}{\mathrm{d}\omega'} \overset{\omega'\to 0}{\longrightarrow} \frac{1}{\omega'} \cdot \sigma_\pi \tag{13}$$

with a weight-averaged total cross section

$$\sigma_\pi = \frac{e^2}{2\pi^2} \int \mathrm{d}\Omega_\pi \, W(v) \cdot \frac{\mathrm{d}\sigma}{\mathrm{d}\Omega_\pi} \tag{14}$$

for the $\gamma p \to p\pi^0$ reaction. From the low-energy theorem of eq. (13), as derived in appendix B of ref. [42], the cross section ratio

$$R = \frac{1}{\sigma_\pi} \cdot \omega' \cdot \frac{\mathrm{d}\sigma}{\mathrm{d}\omega'} \tag{15}$$

is defined, with the soft-photon limit value $R \to 1$ for vanishing photon energies $\omega' \to 0$.

Table 3. Weight-averaged total cross sections σ_π. Theoretical predictions are from the unitary model [33] and the χEFT calculation [35]. Experimental values refer to Crystal Ball / TAPS results with statistical and systematic errors.

Beam energy ω	Weight-averaged cross section σ_π unitary	χEFT	experimental
350 MeV	56.97 nb	60.51 nb	$56.18 \pm 0.06 \pm 2.26$ nb
400 MeV	42.17 nb	51.82 nb	$40.59 \pm 0.06 \pm 1.64$ nb
450 MeV	32.31 nb	49.47 nb	$25.91 \pm 0.07 \pm 1.04$ nb

This ratio is less sensitive not only to experimental uncertainties (*e.g.* photon flux, target density) which contribute to both $\mathrm{d}\sigma/\mathrm{d}\omega'$ and σ_π and hence cancel out in R, but also to inaccuracies in theoretical model calculations of $\gamma p \to p\pi^0$, as this observable depends only on the deviation from the soft-photon behaviour. Quantitative effects of these model dependencies can be estimated through the weight-averaged total cross section σ_π from eq. (14) for the $\gamma p \to p\pi^0$ reaction. Table 3 compares predictions for σ_π from both the unitary model [33] and the χEFT calculation [35] with experimental Crystal Ball / TAPS results obtained from an analysis of $\gamma p \to p\pi^0$ at three different beam energies ω in the considered energy range. While the unitarised effective Lagrangian framework [33] gives good agreement with experimental results at least in the low and medium photon energy range, the χEFT calculation [35] shows discrepancies of about 10% already at low photon energies, increasing to nearly a factor of two at the highest beam energy. As mentioned above, this is due to reaction mechanisms not included in the χEFT expansion and, therefore, a well-understood limitation, which does not affect the description of Δ-resonant processes.

With these results for the weight-averaged cross section σ_π for the non-radiative $\gamma p \to p\pi^0$ reaction and the energy differential cross sections $\mathrm{d}\sigma/\mathrm{d}\omega'$ from fig. 16, cross section ratios R have been derived according to eq. (15) for the three different beam energy ranges (see fig. 18). Also for this observable, the same value for the anomalous magnetic moment κ_{Δ^+} results in significant discrepancies

between the unitary and χEFT predictions. This shows that there is still a remaining model dependence in the description of $\gamma p \to p\pi^0\gamma'$, which does not cancel in R and, therefore, is not related to details of the $\gamma p \to p\pi^0$ reaction model. Such model dependencies, however, limit the accuracy of any values for κ_{Δ^+} extracted from experimental results.

The following considerations and fits to experimental results will concentrate on the medium beam energy range around $\omega = 400$ MeV, as this is a compromise between sensitivity to κ_{Δ^+}, which is fairly low at lower beam energies, and the agreement between experimental data and theoretical calculations, which gets worse with rising beam energy. Such a procedure that uses only a limited part of our experimental results is not suitable for an unambiguous determination of the $\Delta^+(1232)$ magnetic dipole moment, but will still give an impression of the statistical and systematic precision for μ_{Δ^+} that might be achieved if improved theoretical models become available. The left panel of fig. 19 shows a χ^2 fit of unitary model predictions to our new results for R for emitted photon energies up to the kinematic limit at $\omega' \simeq 180$ MeV with the anomalous magnetic moment κ_{Δ^+} as free parameter. This fit gives a result of $\kappa_{\Delta^+} = 2.79^{+0.39}_{-0.44}(\text{stat}) \pm 0.39(\text{syst})$, but the obtained fit quality of $\chi^2/\text{ndf} = 2.94$ (ndf = 28) indicates that, even with the restriction to beam energies around $\omega = 400$ MeV, the agreement between experimental data points and theoretical model calculations in the unitarised effective Lagrangian framework [33] is not sufficient for a reliable extraction of the $\Delta^+(1232)$ magnetic dipole moment. As already mentioned in the discussion of the energy differential cross sections $\mathrm{d}\sigma/\mathrm{d}\omega'$ the model overestimates a peak structure for energies around $\omega' = 60$ to 100 MeV and does not fully reproduce the shape of the experimental distribution.

In the case of the χEFT calculation (see right panel of fig. 19) it is reasonable to limit the fit to emitted photon energies up to $\omega' = 120$ MeV [43], which yields a value of $\kappa_{\Delta^+} = 3.95^{+0.18}_{-0.20}(\text{stat}) \pm 0.85(\text{syst})$ at $\chi^2/\text{ndf} = 2.72$ (ndf = 16). This restriction to low-energy photons γ' is motivated by the expansion schemes used in the χEFT framework, which require the initial beam photon to be in the order of the $\Delta^+(1232)$ excitation energy, while the emitted photon γ' has to be soft. Applicability of this model is, therefore, limited to beam energies not too far away from the resonance point (which gives another reason for ruling out the higher beam energy bin at $\omega =$ 450 MeV), while the low-energy expansion in ω' becomes problematic for γ' energies near the kinematic limit. However, also at low photon energies around $\omega' = 40$ MeV there still remains a discrepancy between the experimental results and the χEFT calculation. Thus, at the moment none of these theoretical descriptions seems to give a precise description of the experimental results that would be needed for a reliable extraction of the anomalous magnetic moment κ_{Δ^+}. Furthermore, the fit results for κ_{Δ^+} obtained from both models are not compatible with each other.

6 Conclusion and outlook

A new measurement of radiative π^0 photoproduction $\gamma p \to p\pi^0\gamma'$ in the $\Delta^+(1232)$ energy region has been performed. The data were obtained with the Crystal Ball / TAPS detectors using an energy-tagged photon beam produced at the electron accelerator facility MAMI-B. Compared to the pioneering TAPS / A2 experiment in ref. [19], from which the $\Delta^+(1232)$ magnetic dipole moment μ_{Δ^+} was extracted for the first time, a considerable improvement on statistics by nearly a factor of 60 has been achieved. This new experiment yielded differential cross sections for both the emitted photon γ' and the π^0 with high resolutions in polar angles $\theta_{\gamma'}$ and θ_π and emitted photon energy ω'. These cross sections show a reasonable agreement with the previous experimental result, but cannot be fully reproduced by different theoretical models [33,35] for $\gamma p \to N\pi\gamma'$ reactions.

Part of this discrepancy vanishes if the cross section ratio R from eq. (15) is evaluated, as this eliminates some of the model dependencies, but also with this observable a reliable and precise extraction of the magnetic dipole moment μ_{Δ^+} seems to be prevented by limitations in the applicability of the models and their inability to describe our experimental data accurately. Thus, substantial progress on the model descriptions is required in order to fully exploit the present experimental results, as the large improvement in the quality of this data compared to the older measurement of radiative π^0 photoproduction reveals shortcomings in the models that previously were not apparent due to the limited statistics in ref. [19]. In this context already different approaches for the on-shell propagator in the $\Delta \to \Delta\gamma'$ process, as they have been recently studied for three models in ref. [44], turn out to have significant influence on both shape and magnitude of the theoretical predictions for $\gamma p \to p\pi^0\gamma'$ cross sections.

In the meantime also several other observables have been suggested that show a larger and more direct dependence on μ_{Δ^+}, *i.e.* not relying on interference effects between the Δ-resonant process and bremsstrahlung contributions. For example, ref. [35] proposes to measure helicity asymmetries Σ_{circ} with a circularly polarised photon beam. These helicity asymmetries are nonzero only for three-body final states and vanish exactly in the the soft-photon limit $\omega' \to 0$, as $\gamma p \to N\pi\gamma'$ processes reduce to $\gamma p \to N\pi$ two-body reactions. Furthermore, Σ_{circ} shows a linear dependence on μ_{Δ^+}, where it should be noted that this is a model-independent feature because of the low-energy theorem for $\gamma p \to N\pi\gamma'$. This model-independent determination of μ_{Δ^+} would require a measurement with a high degree of circular photon beam polarisation in the energy region around the $\Delta^+(1232)$ resonance point. However, as the predicted magnitude of these helicity asymmetries is in the order of only about 1%, such a measurement would require a further major improvement in statistics which seems currently out of reach.

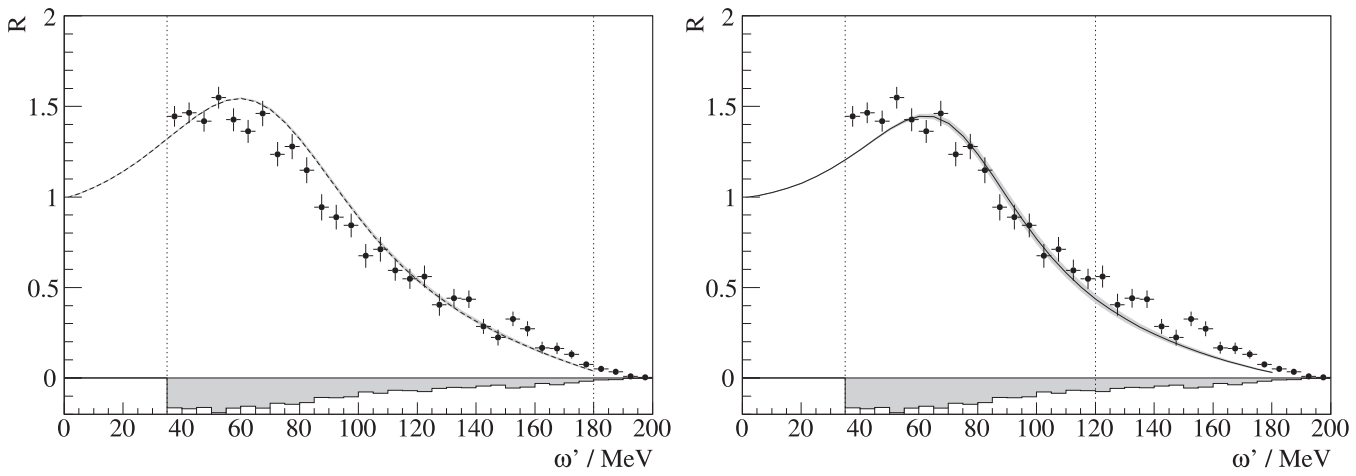

Fig. 19. Cross section ratio R for beam energies from $\omega = 375$ to 425 MeV. The dashed and solid lines represent the best χ^2 fit for the unitary model (left) and the χEFT calculation (right) with κ_{Δ^+} as free parameter. Grey shaded bands show the variations of the model predictions within the statistical fit errors for κ_{Δ^+}, vertical lines indicate the range of emitted photon energies used for fitting.

7 Acknowledgments

It is a pleasure to acknowledge useful discussions with V. Pascalutsa and M. Vanderhaeghen. The authors thank the MAMI accelerator group and operators for their excellent support. This work was supported by Deutsche Forschungsgemeinschaft (SFB 443, SFB/TR 16), DFG-RFBR (Grant No. 05-02-04014), European Community-Research Infrastructure Activity under FP6 "Structuring the European Research Area" programme (Hadron-Physics, Contract No. RII3-CT-2004-506078), Schweizerischer Nationalfonds, NSERC (Canada), UK EPSRC and STFC, US DOE and US NSF. We thank the undergraduate students of Mount Allison University and The George Washington University for their assistance.

References

1. F. Schlumpf, Phys. Rev. **D** 48, (1993) 4478.
2. G.S Yang, H.C. Kim, M.Praszalowicz, K. Goeke, Phys. Rev. **D** 70, (2004) 114002.
3. S.T. Hong, D.P. Min, arXiv:nucl-th/9909004.
4. D.B. Leinweber, T. Draper, R.M. Woloshyn, Phys. Rev. D **46**, (1992) 3067.
5. I.C. Cloet, D.B. Leinweber, A.W. Thomas, Phys. Lett. B **563**, (2003) 157.
6. R. Beck *et al.*, Phys. Rev. Lett. **78**, (1997) 606.
7. S.S. Kamalov, S.N. Yang, D. Drechsel, O. Hanstein, L. Tiator, Phys. Rev. C **64**, (2001) 032201.
8. L.A. Kondratyuk, L.A. Ponomarov, Yad. Fiz. **7**, (1968) 11 [Sov. J. Nucl. Phys. **7**, (1968) 82].
9. D. Drechsel, M. Vanderhaeghen, Phys. Rev. C **64**, (2001) 065202.
10. M. Arman *et al.*, Phys. Rev. Lett. **29**, (1972) 962.
11. B.M.K. Nefkens *et al.*, Phys. Rev. D **18**, (1978) 3911.
12. C.A. Meyer *et al.*, Phys. Rev. D **38**, (1988) 754.
13. A. Bosshard *et al.*, Phys. Rev. D **44**, (1991) 930.
14. L. Heller, S. Kumano, J.C. Martinez, E.J. Moniz, Phys. Rev. C **35**, (1987) 718.
15. R. Wittman, Phys. Rev. C **37**, (1988) 2075.
16. D. Lin, M.K. Liou, Z.M. Ding, Phys. Rev. C **44**, (1991) 1819.
17. G.L. Castro, A. Mariano, Phys. Lett. B **517**, (2001) 339.
18. D. Groom *et al.*, Eur. Phys. J. C **15**, (2000) 1.
19. M. Kotulla *et al.*, Phys. Rev. Lett. **89**, (2002) 272001.
20. Th. Walcher, Prog. Part. Nucl. Phys. **24**, (1990) 189.
21. I. Anthony, J.D. Kellie, S.J. Hall, G.J. Miller, J. Ahrens, Nucl. Inst. Meth. A **301**, (1991) 230.
22. S.J. Hall, G.J. Miller, R. Beck, P. Jennewein, Nucl. Inst. Meth. A **368**, (1996) 698.
23. M. Oreglia *et al.*, Phys. Rev. D **25**, (1982) 2259.
24. A. Starostin *et al.*, Phys. Rev. C **64**, (2001) 055205.
25. R. Novotny, IEEE Trans. Nucl. Sci. **38**, (1991) 379.
26. A.R. Gabler *et al.*, Nucl. Inst. Meth. A **346**, (1994) 168.
27. D. Drechsel, O. Hanstein, S.S. Kamalov, L. Tiator, Nucl. Phys. A **645**, (1999) 145.
28. D. Drechsel, S.S. Kamalov, L. Tiator, Eur. Phys. J. A **34**, (2007) 69.
29. M. Kotulla, PhD thesis, Justus Liebig-Universität Gießen, Germany, 2001.
30. A.I. Machavariani, A. Faessler, A.J. Buchmann, Nucl. Phys. A **646**, (1999) 231.
31. A.I. Machavariani, A. Faessler, A.J. Buchmann, Nucl. Phys. A **686**, (2002) 601.
32. D. Drechsel, M. Vanderhaeghen, M.M. Giannini, E. Santopinto, Phys. Lett. B **484**, (2000) 236.
33. W.T. Chiang, M. Vanderhaeghen, S.N. Yang, D. Drechsel, Phys. Rev. C **71**, (2005) 015204.
34. V. Pascalutsa, M. Vanderhaeghen, Phys. Rev. Lett. **94**, (2005) 102003.
35. V. Pascalutsa, M. Vanderhaeghen, Phys. Rev. D **77**, (2008) 014027.
36. V. Pascalutsa, D.R. Phillips, Phys. Rev. C **67**, (2003) 055202.
37. V. Pascalutsa, M. Vanderhaeghen, Phys. Rev. D **73**, (2006) 034003.

38. R.A. Arndt, I.I. Strakovsky, R.L. Workman, Phys. Rev. C **53**, (1996) 430.
39. A.V. Sarantsev *et al.*, Phys. Lett. B **659**, (2008) 94.
40. J. Ahrens *et al.*, Phys.Lett. B **624**, (2005) 173.
41. R. Leukel, PhD thesis, Johannes Gutenberg-Universität Mainz, Germany, 2001.
42. W.T. Chiang, S.N. Yang, M. Vanderhaeghen, D. Drechsel, Nucl. Phys A **723**, (2003) 205.
43. M. Vanderhaeghen, private communication.
44. A.I. Machavariani, A. Faessler, Phys. Rev. C **72**, (2005) 024002.